Lawrence Berkeley National Laboratory

Title
Monolithic Photoelectrochemical CO2 Reduction Producing Syngas at 10% Efficiency

Authors
Kistler, Tobias A
Um, Min Young
Cooper, Jason K
et al.

Monolithic Photoelectrochemical CO$_2$ Reduction Producing Syngas at 10% Efficiency

Tobias A. Kistler[1,2,3], Min Young Um[1,2], Jason K. Cooper[1,2], Ian D. Sharp[3], Peter Agbo[1,2,*]

[1]Chemical Sciences Division, Lawrence Berkeley National Laboratory, Berkeley, California, USA

[2]Joint Center for Artificial Photosynthesis, Lawrence Berkeley National Laboratory, Berkeley, California, USA

[3]Walter Schottky Institute and Physics Department, Technische Universität München, Garching, Germany

[*]Corresponding Author: pagbo@lbl.gov

Keywords

Abstract

Increasing anthropogenic carbon dioxide (CO_2) emissions have prompted the search for photoelectrochemical (PEC) methods of converting CO_2 to useful commodity products, including fuels. Ideally, such PEC approaches would be sustained using only sunlight, water, and CO_2 as energetic and reactant inputs. However, low peak conversion efficiencies (< 5%) have made commercialization of fully-integrated PEC devices prohibitive. Here, we report a 4 cm^2 monolithic PEC device exceeding 10% solar-to-fuel efficiency with principal fuel products of carbon monoxide (CO) and hydrogen (H_2). The corresponding solar-to-CO and solar-to-H_2 efficiencies are 7% and 3.5%, respectively. Screening of a range of operating conditions revealed a tunable product mixture of H_2 and CO using a gold electrocatalyst. Accordingly, we show that device optimization enabled us to yield a H_2-to-CO ratio of 1:2 commonly present in synthesis gas (syngas). Notably, the modularity and facile fabrication of this device permit the incorporation of a broad array of materials for various applications. For example, the electrocatalyst may easily be swapped to target a different set of products.

1. Introduction

A steady increase of anthropogenic carbon dioxide (CO_2) emissions since the industrial revolution, coupled with the persistence of this greenhouse gas in the atmosphere over geological timescales, has prefigured our current climate crisis.[1,2] Critical increases in mean planetary temperature, resulting from CO_2 release, are projected to occur over relatively short timescales, mandating active management of human CO_2 emissions to limit global warming to 2 °C by 2050.[3] Barring significant advancements in carbon-neutral or carbon-negative energy technologies, scalable approaches for CO_2 mitigation will remain intractable as atmospheric CO_2 concentrations continue to rise.

An appreciation for this reality has motivated the development of carbon-neutral/negative processes, such as CO_2-derived fuels/materials production, capable of displacing their carbon-positive counterparts across all economic sectors. CO_2 reduction reactions generally enable a wide range of mixed products,[4] mostly depending on the catalyst, its surface structure and the electrolyte,[5-14] often requiring downstream separation. However, carbon monoxide (CO) and its mixture with hydrogen (H_2), called synthesis gas (syngas), may be obtained at a selectivity higher than 90%.[15] Syngas is an important precursor in the chemical industry for the production of alcohols,[16] acetic acid[17] and synthetic hydrocarbon fuels[18,19] but is typically produced from fossil fuels. Alternatively, CO_2 reduction may be driven by electricity from renewable sources, such as solar cells, significantly lowering its carbon footprint.[20-22]

In solar-driven CO_2 electrolysis (artificial photosynthesis),[23] the solar-to-fuel efficiency marks a critical figure-of-merit, describing the efficiency with which incident solar energy is incorporated into the chemical bonds of a particular fuel or fuel mixture. Recently, solar-to-fuel (STF) efficiencies of 19% at 1 sun illumination intensity have been achieved in devices featuring physically separated photovoltaic (PV) and electrolyzer components.[24-29] However, the state of monolithic, photoelectrochemical (PEC) devices has lagged behind the performance of PV-electrolyzers, with

monolithic architectures to date displaying peak STF efficiencies of 4.6% for solar CO_2 conversion.[30-32] Monolithic designs do not require any wiring between PV and electrocatalytic components during unbiased, photoelectrochemical operation.[33] The challenge of constructing robust, monolithic PEC devices is compounded by the requisite integration of the PV in the electrolysis compartment, limiting the choice of photoabsorber materials to those resistant to corrosion by the alkaline electrolytes generally employed in CO_2 electrolyzers.[34] Despite such constraints, PEC monoliths may benefit from a more compact device design, enabling lower charge transport losses, and favorable heat-exchange between the PV and the electrolyzer,[33] especially under light concentration.[35]

This work describes a monolithic PEC device that converts CO_2 to syngas at a record STF efficiency above 10% (combined solar-to-CO and solar-to-H_2 efficiency). This benchmark represents a doubling in the reported peak efficiency for such devices to date,[31,32] with no efficiency degradation during a 24-hour durability test. However, long-term operation may change the product distribution, leading to increased H_2 evolution over time. Enhanced adhesion of the gold catalyst to the carbon paper substrate is shown to stabilize the product distribution. While solar-driven CO_2 reduction is commonly limited to active areas of 1 cm^2 or less, we demonstrate a straightforward scale-up from 1 to 4 cm^2.[26,27,31] Separation of anode and cathode products is achieved through employment of an ion-exchange membrane, reducing the risk of product re-oxidation at the anode.[31] Preferable operating conditions were found through a systematic analysis of the operating voltage, electrolyte concentration and flow rate, as well as water content and CO_2 flow rate of the cathode feed.

2. Results and Discussion

2.1 Device architecture

The PV-integrated membrane (PIM) provides a unique, compact structure similar to conventional membrane-electrode assemblies (MEAs) used in commercial, grid-based electrolyzers and is the center of our PEC device (**Figure 1**). MEAs typically consist of an ion-exchange membrane closely contacted by electrocatalysts and gas diffusion layers (GDLs).[36-38] MEA-type devices display lower operating voltages than corresponding flow cells and have the potential to enhance operational stability.[34,39] However, to date no MEA-style, PEC device has been reported for CO_2 reduction.[40]

A humidified feed of high-purity CO_2 is supplied to the device cathode via a bubble humidifier, where it is electrochemically reduced to CO on a gold (Au) catalyst layer deposited on carbon paper (the GDL). H_2 evolution competes with the reduction of CO_2, resulting in a product mixture of CO and H_2. Both reactions produce hydroxide ions, which diffuse through the anion exchange membrane (Selemion AMV) to the anode side of the cell, where they react to oxygen (O_2) over an iridium (Ir) catalyst supported by carbon paper. Acrylic endplates compress the two carbon paper sheets against the membrane, forming a compact MEA,[34] with catalytic areas of 1 cm^2 each for dark experiments and 4 cm^2 each for PEC testing.
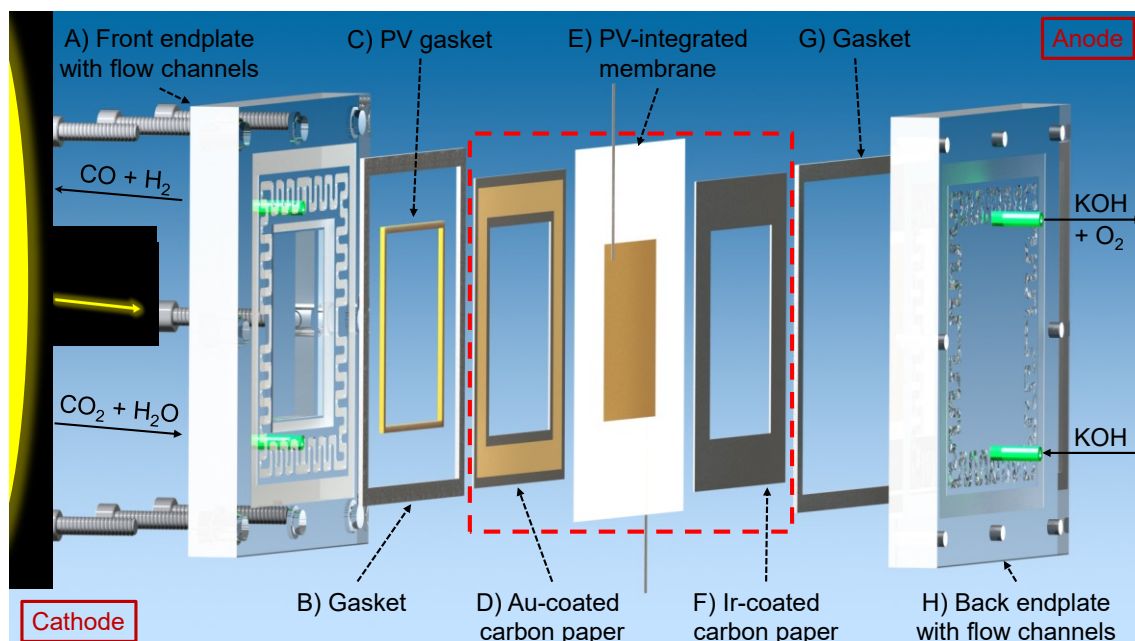
Figure 1. Exploded view of the monolithic PEC device, enclosing the PV-integrated membrane

(PIM). The membrane-electrode-assembly marked in red is featured in **Figure 3** as a cross-section image. We note that the cathode outlet stream also contains unreacted CO_2.

2.2 Dark electrochemical operation

The modularity of our device allows us to bypass electrical connections to the PV and run the electrolyzer as a dark, electrochemical cell. This facilitated the optimization of conditions for solar-driven device operation. Biasing the dark cell at voltages and currents, bounded by the output characteristics of the PV (see Experimental Section) used to drive the final PEC device, served as an effective surrogate for expected PEC cell behavior under solar illumination.

Favorable operating conditions were explored under potentiostat bias, with the goal of generating a syngas product at H_2-to-CO ratios near 0.5, while maximizing CO_2 utilization (see Experimental Section) and yielding a stable cell performance. A syngas product ratio of 0.5 may, for example, serve as a feedstock for a downstream Fischer-Tropsch process, producing synthetic fuels on iron catalysts.[19] For this study, the main parameters of interest were the full cell voltage, the temperature of the bubble humidifier which controls the water content of the cathode feed, the concentration and flow rate of the anode electrolyte (anolyte) and the CO_2 flow rate. Unless otherwise mentioned, the humidifier temperature was set to room temperature (25 °C), a 1M potassium hydroxide (KOH) solution supplied at a rate of 0.05 ml min^{-1} constituted the anolyte feed, and the CO_2 flow rate at the cathode was 10 sccm. Stability measurements were carried out for three hours and the average values during the last 90 min are displayed in **Figure 2**.

Full cell voltage dependencies were explored by varying the cell bias from 2 to 3 V, in 0.25 V increments. Application of higher voltages results in linear increases of the current density, typically skewing the product distribution of the resulting fuel stream towards H_2 (**Figure 2**a).[18,27,41,42] Despite enhancements in CO_2 utilization efficiencies with increasing current density, the H_2-to-CO ratio also

6

rises linearly from 0.07 at 2 V to 1.05 at 3 V. The targeted syngas ratio of 0.5 may be achieved just below 2.5 V, at a projected current density of approximately 15 mA cm^{-2}. In all cases, the measured current density, given with respect to the catalyst geometric surface area, exhibited good stability following an approximately 15 min settling period (Supplementary Figure S1).

The influence of the humidifier temperature was examined at a constant current density of 12 mA cm^{-2}, an operating condition that could be expected for a PEC device running under non-concentrated illumination (see Experimental Section). The humidifier temperature is found to display relatively little influence on the resultant H_2-to-CO ratio and CO_2 utilization efficiency at temperatures between 25 and 60 °C (**Figure 2**b). However, sufficiently high humidification temperatures (80 °C) result in water condensation in the cathode compartment of the unheated electrochemical cell due to the significant temperature differential between the cathode chamber and humidifier. Thus, as condensation increases, the cell conditions approach those of a liquid-fed cathode, significantly reducing the effective CO_2 concentration at the Au catalyst layer (Supplementary Table S1). Consequently, the product ratio is found to shift considerably towards H_2 evolution, causing drops in single-pass CO_2 utilization while increasing the H_2 crossover through the membrane (Supplementary Figure S2). As a result of these observations, coupled with the desire to operate the device with minimal energy input, 25 °C was chosen as the desirable humidifier temperature.

The concentration of the potassium hydroxide anolyte significantly influences the device performance, evidenced by the results of anolyte concentrations between 0.001 to 1M (**Figure 2**c and Supplementary Figure S3). At the lowest investigated concentration of 0.001M, the chosen current density of 12 mA cm^{-2} can only be sustained at a very high cell voltage. Choosing an operating voltage of 3 V, instead of a constant current, ensured that product gas concentrations remained above the detection limit at all test points, limiting the experimental error, while maintaining comparability within this concentration test series. The current density is found to scale

as a linear function of the anolyte concentration. Higher current densities lead to an increased local pH at the catalytic sites, favoring H_2 evolution[43,44] and significantly raising the H_2-to-CO product ratio. The CO_2 utilization displays asymptotic behavior with respect to increasing anolyte concentration: gradual improvements in CO_2 usage transition to a plateau region beyond 0.5м KOH. To ensure sufficient electrolyte conductivity, we chose 1м KOH as the electrolyte for subsequent experiments. Higher anolyte concentrations would result in an excessively caustic environment, as 1м KOH already yields current densities significantly above 12 mA cm^{-2} at 3 V applied bias. The large H_2-to-CO ratio and the minor, corresponding increase in current density of this sample follows the observed trend with increasing KOH concentration, and is likely a consequence of operating the Au catalyst at a large applied voltage of 3 V, which was used in this test series, as described above. Au is known to change its surface atomic arrangement under voltage bias,[45] potentially altering the product selectivity in CO_2 reduction.[46]

Increasing the anolyte flow rate 5-fold did not affect the device performance considerably but increased the CO_2 membrane crossover (Supplementary Figure S4). These results highlight the importance of incorporating substrate crossover in the determination of the maximum achievable CO_2 utilization.[34] Decreasing the anolyte flow rate by a factor of 10 caused dehydration of the anion-exchange membrane, lowering its conductivity and consequently increasing the operating voltage.

In an effort to optimize CO_2 utilization, the CO_2 flow rate was reduced in steps of 2 sccm (**Figure 2**d). At 2 sccm, the utilization is enhanced by a factor of four relative to experiments performed at 10 sccm. However, at 2 sccm, the H_2-to-CO ratio is directed towards enhanced H_2 evolution as the concentration of CO_2 decreases relative to the water availability at the catalyst-ionomer interface.[47,48] The targeted ratio of 0.5 was achieved at a CO_2 flow rate of 10 sccm with a utilization efficiency of 0.6%. To obtain greater CO_2 utilization efficiencies, the operating current

8

would need to be increased significantly while keeping the remaining parameters constant (Supplementary Figure S5).

Furthermore, switching the cathodic CO_2 feed to a humidified argon feed showed no CO production (Supplementary Figure S6), with the only cathodic reaction being H_2 evolution, indicating that CO is only formed through genuine reduction of CO_2. Under the conditions tested, this control experiment also indicated that H_2 evolution shows a higher onset potential than CO_2 reduction, while current densities above 10 mA cm^{-2} could be sustained at a lower voltage without the presence of CO_2. Finally, a $^{13}CO_2$ labeling experiment confirmed that all of the produced CO is generated from the CO_2 input (Supplementary Figure S7).

Through careful selection of the operating conditions, the targeted H_2-to-CO ratio of 0.5 was achieved at a constant generation rate. Different product ratios are readily available by changing the water content or flow rate of the cathode CO_2 feed. Our results indicate that reactant concentrations at catalyst active sites significantly influence product selectivity. Furthermore, increasing the operating voltage and current density significantly shifts the product ratio to favor H_2. However, in an integrated PEC device, these parameters are generally limited by the characteristics of the solar cell and electrocatalyst. While CO_2 utilization rates remained below 3% for all parameter combinations tested, CO_2 flow rates between 2-4 sccm displayed an exponential increase in utilization in the limit of ultra-low CO_2 flow rates. However, H_2 evolution is expected to dominate at such flow rates. Such findings suggest that low concentration CO_2 gas streams, such as air or flue gas, could be supplied to the cathode at 10 sccm, reducing the amount of CO_2 in the feed,[49] while limiting H_2 evolution by keeping the water content low. In this case, it would be necessary to employ a catalyst that prevents reactions of other components than CO_2 present in air or flue gas, such as the oxygen reduction reaction. This possibility remains a focus of ongoing investigations.
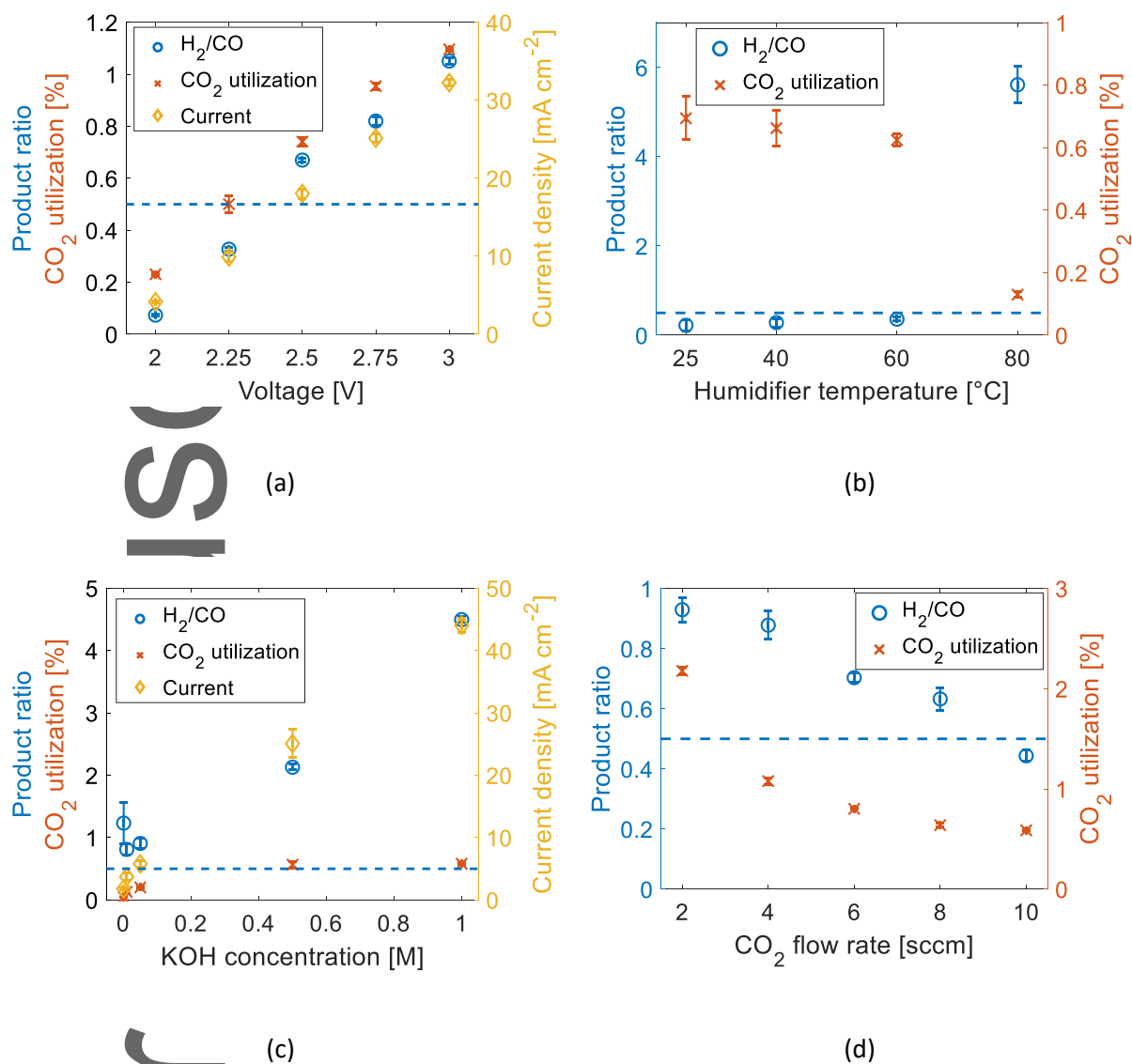
Figure 2. Variation of operating conditions in a dark, electrochemical cell. The current density values are based on the geometrical surface area of the catalyst (1 cm^2). All displayed data points were determined by averaging the measured values, obtained during the last 90 minutes of 3 h stability tests, while error bars mark their standard deviations. The horizontal dashed lines indicate the target H$_2$-to-CO ratio of 0.5 for the syngas product. (a) Applied cell voltage. (b) Temperature of the cathode bubble humidifier, at a constant current density of 12 mA cm^{-2}. (c) Potassium hydroxide (KOH) concentration of the anode feed, at a constant voltage of 3 V. (d) CO$_2$ cathode flow rate, at a constant current density of 12 mA cm^{-2}.

2.3 Photoelectrochemical operation

A four-junction PV is integrated into the Selemion membrane to enable wireless, photoelectrochemical operation. As previously reported,[33,50] we note that the metallic contact foils attached to the PV shown in **Figure 1** are not necessary for PEC operation but are only integrated for diagnostic purposes (see Experimental Section for details). The PIM is then sandwiched between catalyst-coated carbon papers, similar to the dark, electrochemical experiments described above. As a result of the PV size (2 x 2 cm^2), the catalytic area was scaled up to 4 cm^2 during PEC operation.

The PIM device enables beneficial illumination through the cathode, reducing path-dependent light attenuation between the light source and PV, relative to other designs that include elements such as electrolytes or catalysts in the illumination path.[30- 32] The photons from the light source only need to pass through the transparent front endplate, before being absorbed by the PV. The photogenerated electrons drift towards the front contact of the PV, while the holes are collected at the back of the PV, driving the electrochemical reactions occurring at the catalyst surfaces (**Figure 3**a).

Since the catalytic area is concentric about the PV, it could be argued that illumination area is lost to the dark catalyst surface. However, a Fresnel lens[51] the size of the PV plus surrounding catalyst may concentrate the light on the PV, making full use of the available surface area (**Figure 3**b). We note that the operating conditions of the PEC device described in **Figure 2** would then need to be matched appropriately to the higher light intensity using the method described above for determining the key output characteristics as a function of device operating conditions. For a concentration cell, these would need to be determined as a function of light intensity since the increased device temperature due to light concentration is expected to alter the product ratio by

influencing the relative humidity in the cell. At the same time, the CO_2 utilization efficiency likely increases with higher operating currents, while keeping the CO_2 inlet flow rate constant.

(a)   (b)
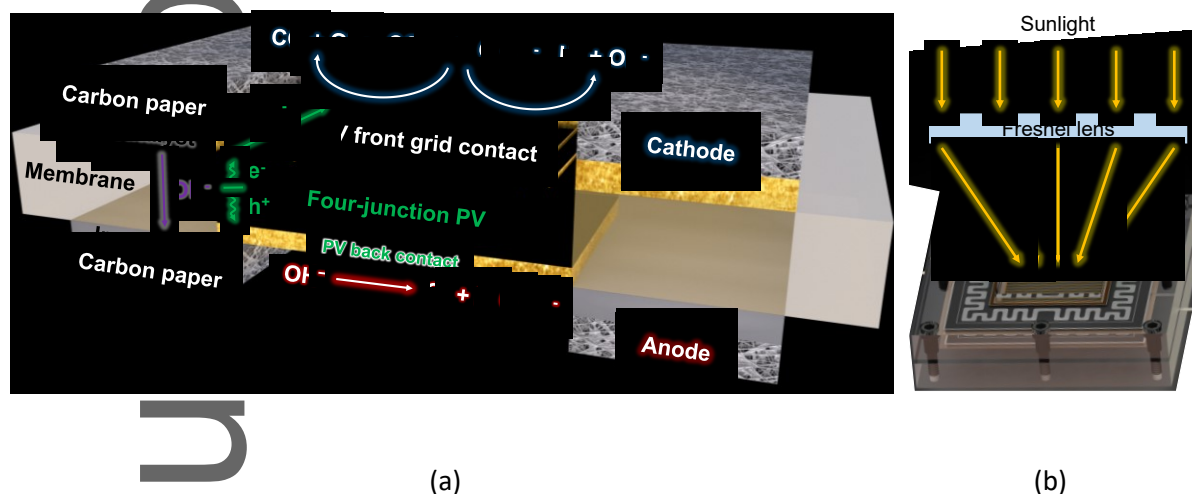
Figure 3. Monolithic PEC device structure (a) Cross-section view at the device's active components, such as PIM and catalyst-coated carbon papers, highlighting the charge generation and transport processes. The thicknesses of the layers are not to scale, and the chemical reactions are shown without coefficients. (b) Schematic depicting the potential use of a Fresnel lens, concentrating the sunlight on the photoactive parts of the PEC cell.

The stability of the PEC cell was tested for three hours under unbiased conditions for spontaneous overall CO_2 reduction, showing a near constant current density of approximately 8.8 mA cm^{-2} (**Figure 4**a), which is close to the short-circuit current density of the PV under terrestrial AM1.5G illumination conditions (Supplementary Figure S8). The full cell voltage during this test was near 2.8 V at the beginning, then declined quickly to 2.2 V within 15 minutes due to electrode conditioning effects (Supplementary Figure S8). During operation, an increase in electrode activity is observed, as indicated by a steady decrease in operating voltage. The cause of this gradual increase in activity is assigned to anolyte diffusion through the membrane, which results in improved wetting

12

of the cathode catalyst layer. This effectively increases the contact area between the Au catalyst layer and the ionomer, reducing the cathodic overpotential required for device operation.[44] Accordingly, electrochemical impedance spectroscopy (EIS) shows a continuous drop of the polarization resistance during conditioning, while the series resistance remains constant (Supplementary Figure S9). To prove that the Au electrode is the conditioned component, a control experiment, where all electrochemically-active components were replaced sequentially for fresh components after conditioning, was carried out. Replacement of Ir catalysts and membranes did not change the performance significantly, while a fresh Au electrode required repeated conditioning (Supplementary Figure S10). The result of the conditioning process was a reduced operating voltage after 15 minutes while the current remained stable since it is limited by the PV output. Finally, the voltage stabilized around 2.25 V, marking a significant gap between the operating voltage and the voltage of the PV at its maximum power point (MPP, 3.1 V).

The gap between the operating voltage and the MPP of the PV indicates that the electrocatalysts are under-utilized and provides an opportunity to run the PEC cell at higher currents through solar concentration. The elevated light intensity would increase the short-circuit current of the PV and thus the STF efficiency but is more demanding on the catalysts which need to support the higher current density (Supplementary Figure S11). Alternatively, earth-abundant catalysts that require higher overpotentials than precious metals such as Ir and Au may reduce the system costs. Both higher current densities and increased catalyst overpotentials would increase the operating voltage of the full device. However, as long as the voltage stays below the maximum power point of the PV, the 10% STF efficiency measured for this system should not be impacted appreciably.

Faradaic efficiency measurements from the unbiased device operation indicate a H_2-to-CO ratio near 0.5, with ~90% of the measured current stored in syngas product (**Figure 4**a). According to the faradaic efficiencies, mean partial current densities for CO and H_2 are calculated to be 5.53 ± 0.46 mA cm^{-2} and 2.26 ± 0.43 mA cm^{-2}, respectively. Maintaining a 10 sccm CO_2 flow rate, while

13

increasing catalytic areas of the PEC device by a factor of 4 relative to the dark cell experiments, is found to boost the CO_2 utilization efficiency from 0.6 to 1.6% (Supplementary Figure S8). Reports of solar-driven CO_2 electrolyzers usually do not mention the CO_2 utilization efficiency, but it may be calculated from the published results and associated operating conditions.[49,52] Our calculations (Supplementary Table S2) show that many notable devices[24,26,27,29,31,49,53-56] exhibit CO_2 utilization efficiencies below 1%. Given the clear relevance of CO_2 utilization efficiency to the field of (photo-)electrochemical CO_2 reduction, disclosure of this metric should become standard practice for future reports on CO_2 reduction devices.

The liquid-gas separator behind the anode outlet was first flushed with nitrogen two hours after the start of the experiment, marking the beginning of the O_2 concentration measurement. Faradaic efficiencies for O_2 evolution stabilized around 90% one hour after the initial concentration measurement. The stoichiometry of anodic and cathodic products matches well when their cumulative faradaic efficiencies of ~90% each are compared. However, the missing 10% cannot be solely explained by H_2 crossover from the cathode through the membrane to the anode. In particular, quantification indicates that only $1 - 2\%$ of current is lost to H_2 crossover during the course of the test (Supplementary Figure S8). Furthermore, negligible amounts of CO were detected in the anode and liquid products were not observed in the cathode. However, if the cathodic products end up in the anode compartment, they may easily be re-oxidized. Such a parasitic process would consume charge carriers in the anode, masking any cathodic product crossover before downstream chromatographic detection, while explaining the reduced faradaic efficiency for O_2.

With the measured current density and the faradaic efficiencies for CO and H_2 products, the respective solar conversion efficiencies may be calculated, which indicate the energy quantities stored in the product gases, compared to the input light energy. After 3 hours of PEC operation, the solar-to-hydrogen (STH) efficiency stabilizes at approximately 3.5%, while the solar-to-CO efficiency reaches 7% (**Figure 4**b). The sum of these individual efficiencies yield a combined solar-to-fuel (STF)

14

efficiency that exceeds 10% throughout the three-hour experiment. While this marks a doubling in peak STF efficiency for monolithic devices, the product generation rate and CO_2 utilization efficiency is also enhanced compared to two of the best-performing devices reported to date (Table S3).[30,31]

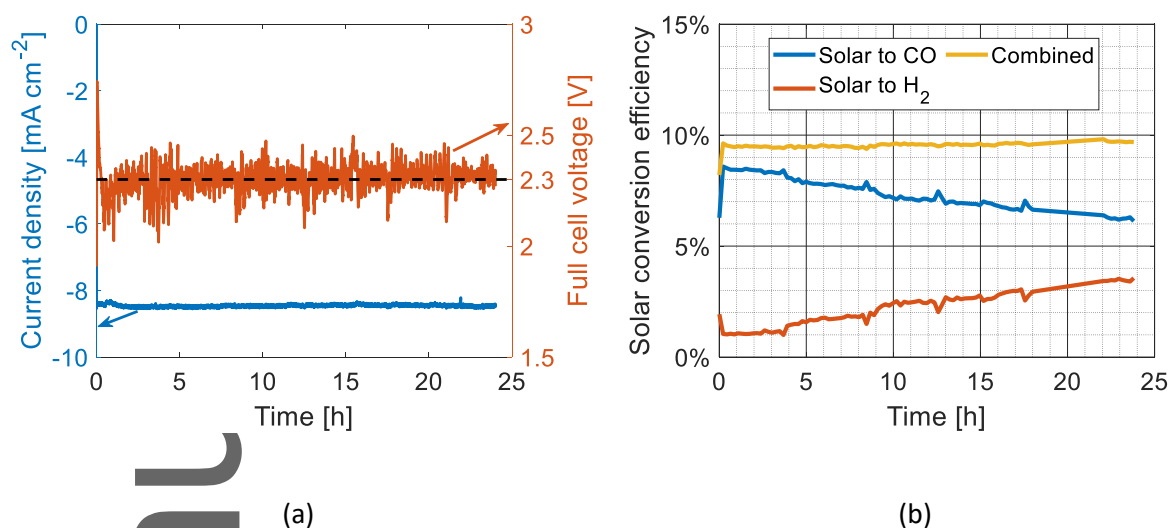(a)   (b)
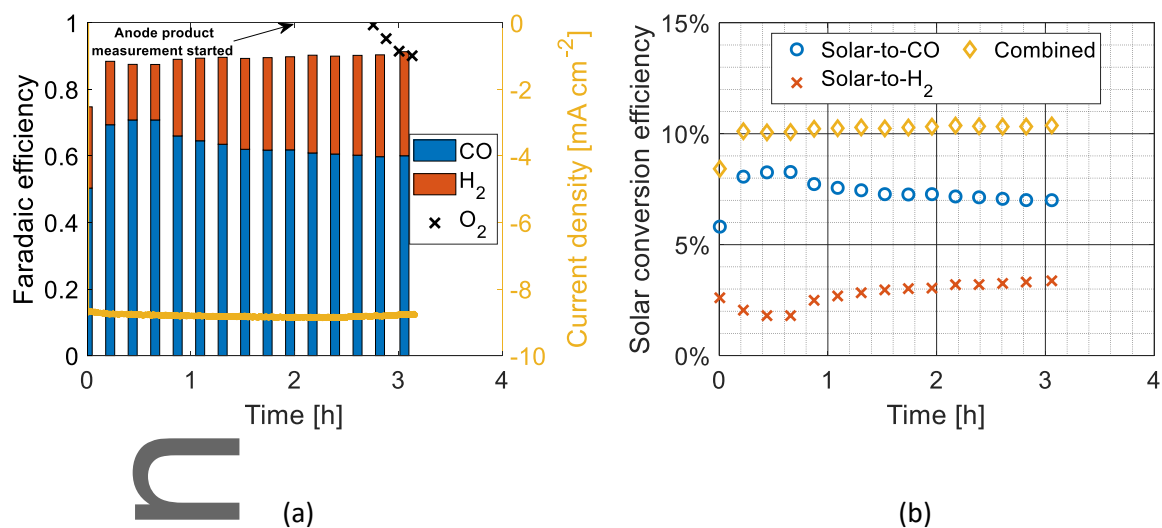
Figure 4. Unbiased PEC operation under simulated AM1.5G solar illumination at an intensity of 1 sun. (a) Faradaic efficiency of the product gases and measured current density of the 4 cm^2 device. The current density is based on the geometric surface area of the PV. O_2 concentrations were first measured after 2 hours. During the first four O_2 measurements, air remained in the anode liquid-gas separator, preventing quantification of evolved O_2. Only those values obtained at later times after elimination of remnant air, which resulted in stabilization of the faradaic efficiency at physically reasonable values below 1, are shown. (b) Solar conversion efficiencies of the cathodic product gases.

2.4 Long-term operation and stability analysis

We tested another PIM assembly for an extended 24-hour period, which again resulted in a stable STF efficiency near 10% throughout the experiment (Figure 5 and Supplementary Figure S12).

This test also indicated, that during long-term operation the product distribution may shift towards increased H$_2$ production.

(a)   (b)

Figure 5. Unbiased, 24-hour PEC operation under simulated AM1.5G solar illumination at an intensity of 1 sun. A fresh PV-integrated membrane was used for this test. (a) Real-time current-voltage data during this PEC stability test reveal a fast conditioning process, quickly dropping the operating voltage from 2.7 to 2.3 V, similar to the 3-hour test shown in Figure 4 and Supplementary Figure S8. The current density is based on the geometric surface area of the PV. (b) The combined solar-to-fuel efficiency remains near 10% throughout this run, while the product ratio slowly shifts towards more H$_2$ production.

Previous reports have highlighted that carbon paper is often contaminated with trace quantities of Fe, Co, Ni or Mo[57-60], known catalysts for H$_2$ evolution. However, energy dispersive x-ray spectroscopy (EDS), X-ray photoelectron spectroscopy (XPS) and ion scattering spectroscopy (ISS) showed no clear evidence of carbon paper contamination by adventitious metals (Supplementary Figure S13-S18). XPS and ISS confirm that KOH electrolyte is crossing the membrane from the anode to the cathode during operation as potassium was found on the cathodic carbon paper

16

(Supplementary Figure S18). A more likely cause for the changing product distribution is the delamination of the Au catalyst from the Toray carbon substrate, as evidenced by scanning electron microscopy (SEM) and EDS (Supplementary Figure S13-S17). After delamination, the Au redeposits on the membrane (Supplementary Figure S19). The detachment of the Au catalyst from the carbon paper and its adhesion to the membrane may impede CO_2 from reaching some of its active sites, increasing the chances for H_2 evolution, which only requires protons as a reactant. In such an operation regime, the Au catalyst on the membrane may be approximated as a flooded catalyst layer, resulting in high mass-transport resistances for gaseous reactants.[44]

Therefore, catalyst delamination needs to be avoided. Electron-beam physical vapor deposition (EBPVD) of Au resulted in the same delamination issues (Supplementary Figure S20) experienced with sputter-deposited Au. However, various deposition methods or surface treatments may be employed to avoid the delamination of Au, including the sputter deposition of a 10 nm Ti adhesion layer. Introduction of the Ti adhesion layer is found to significantly mitigate Au delamination from the carbon paper (Supplementary Figure S21-S22), resulting in a stable cathode product ratio. However, our initial results also indicate that these conditions tend to favor H_2 production from the beginning (Supplementary Figure S23). Therefore, stabilizing favorable product yields will require detailed exploration of other surface treatments or deposition techniques in the future.

3. Conclusion

For the first time, a solar-to-fuel efficiency higher than 10% was demonstrated for monolithic, photoelectrochemical CO_2 reduction, doubling the peak efficiency of such devices. The high efficiency was achieved through a compact device architecture (inspired by commercial electrolyzers) which greatly reduces the transport distance for ions. Device optimizations were

17

facilitated by exploring a range of operating conditions, with favorable parameters yielding a targeted H_2-to-CO ratio of 1:2. The primary components of the PIM testbed – membrane, photovoltaic, catalyst and catalyst support materials – are all exchangeable, depending on the specific goal of the application. For example, different electrocatalysts can be used to target different chemical products, such as hydrocarbons, or PVs made from earth-abundant materials may be employed to reduce the costs of the device. In addition to its modularity, the PIM fabrication process is relatively facile, enabling a straightforward device scale-up from 1 to 4 cm^2. Finally, although the 2% CO_2 utilization rate reported here is significantly higher than previous reports, it requires further optimization in order to satisfy the demands of commercial use. Such options may include recycling the unreacted CO_2, the implementation of low-concentration CO_2 feeds such as air or flue gas, or the development and incorporation of catalysts with higher specificities for CO_2 conversion relative to proton reduction. Additionally, larger device areas, light concentration or series-connection of devices may be necessary to obtain significant utilization rates. Such advancements will facilitate the transition from lab-scale demonstrations to industrial commercialization of this technology.

4. Experimental Section

Catalyst deposition

Untreated Toray TGP-H-60 carbon paper from Alfa Aesar with a thickness of ~0.2 mm and porosity of ~80% was used as the catalyst substrate. The gold and iridium catalysts were deposited by radio frequency (RF) sputtering in a five-gun magnetron system from AJA International, Inc. Temperature-stable, 3D-printed plastics (CPE+ from Ultimaker) were used to appropriately mask the regions of carbon paper during sputter deposition, resulting in catalytic areas of 1 and 4 cm^2, respectively. In each case, the carbon paper was slightly larger than the catalytic area to improve robustness. After

18

masking, the carbon paper was cleaned for five minutes via plasma etching in an argon atmosphere at 30 mTorr and 15 W. Immediately after the cleaning step, Ir or Au catalyst layers were deposited in an argon plasma at 3 mTorr and 150 W until a thickness of 100 nm was reached, resulting in catalyst loadings of 0.23 mg cm^{-2} for Ir and 0.19 mg cm^{-2} for Au. The respective deposition rates were determined prior to sputtering, using a quartz crystal microbalance.

Solar cell parameters

Four-junction space PVs (Z4J) from Solaero Technologies, Corp. were used in this study to drive the electrochemical reactions. Each of the four layers of the solar cell responds to different parts of the solar spectrum, and their series-connection results in a higher photovoltage than achievable with a single-junction PV.[61] The increased photovoltage is needed to overcome the relatively high overpotentials generally required for electrochemical CO_2 reduction.[5,30,62] The bare PV parameters such as short-circuit current density (12 mA cm^{-2}) and open-circuit voltage (3.95 V) were measured under AM0 spectral irradiation at 0.135 W cm^{-2} by the manufacturer. Space solar cells are generally characterized using the AM0 light spectrum, which refers to the conditions outside of the Earth's atmosphere. The illumination intensity under 1 sun AM0 conditions is roughly 1.35 times higher than under the terrestrial AM1.5G spectrum (0.1 W cm^{-2}), leading to higher PV parameters compared to AM1.5G conditions. Under AM1.5G illumination conditions and at the typical PEC operating temperature (40 °C), the short-circuit current density is 8.8 mA cm^{-2} and the open-circuit voltage is 3.71 V. The PV fill factor is 0.81 and the PV efficiency is 26% (Supplementary Figure S8). The smallest available PV size was 4 cm^2. To avoid performance losses, we refrained from PV dicing. Although a high-performance multi-junction PV element was chosen for this study, we note that alternative PVs made of abundant elements deposited at low cost may readily substitute the chosen PV, as long as they provide the necessary photovoltage.

Fabrication of the PV-integrated membrane (PIM)

We used Selemion AMV membranes (chloride form, ~0.1 mm thick) from AGC Engineering for this study. The anion-exchange membranes were left untreated and stored in deionized water prior to electrochemical operation or fabrication of the PV-integrated membrane (PIM). Generally, the dark electrochemical devices were assembled using wet membranes but the making of the PIM required dry membranes to achieve good results during the epoxy steps. After drying at room temperature, a square hole approximately the size of the solar cell, was cut into the membrane. Then, the solar cell was fastened with epoxy (3:1 mixture of EPO-TEK 302-3M and LOCTITE Hysol 9460) into the hole of the membrane. Tantalum metal strips were attached to the PV front and back contacts, enabling PV performance evaluation, as well as current logging during photoelectrochemical operation. Tantalum was chosen for its inert characteristics in many different environments and metallic Ta is not expected to catalyze the given electrochemical reactions under the conditions investigated in this work. The contact strips are not essential for operation of the fully-integrated PEC device. However, their incorporation enables measurement and subsequent compilation of performance metrics, such as current and voltage, which provide additional insight into the device behavior during operation.[33,50] The epoxy process requires oven drying steps at 60 °C and has been previously described in detail by the authors.[33] In addition to covering the PV front surface with a transparent epoxy (302-3M), the PV back was also covered with chemical-resistant epoxy to protect it from the harsh basic conditions at the anode. Pinholes of the epoxy should be avoided as much as possible, to prevent corrosion or shunting of the PV. Upon re-humidification, the ionic conductivity of the membrane was sufficient to enable stable device operation, indicating that the drying process did not severely damage the membrane.

Cell assembly

The back endplate was machined from polymethylmethacrylate (PMMA) and positioned on the mounting platform with the serpentine flow channels facing upwards. The serpentine channels extend the path length for the reactants, increasing the substrate-catalyst contact area to favor higher CO_2 utilization rates.[63] After centering the silicone gasket on the respective slot in the endplate, the Ir-coated carbon paper is placed on the flow channels, being surrounded by the gasket. The anode chamber was completed by putting the Selemion membrane on top of the carbon paper and gasket. For the case of the dark mockup cells, the membranes were wet during assembly, while the PV-integrated membrane was dry as a result of the fabrication process. If applicable, the PV was centered at the square hole, encompassed by the anodic carbon paper. The cathode assembly mirrors the anode, but with the Ir catalyst replaced by a Au catalyst. After positioning the Au-coated carbon paper and the silicone gasket, the front endplate was gently pushed on the remaining cell parts. For the case of the PEC cell, a gasket concentric about the PV perimeter was used to enhance compression and minimize condensation at the PV front. Finally, the screws were inserted in the respective slots of the front endplate and tightened to the back endplate in a star-shape manner to a torque of 0.1 N m, resulting in uniform compression of the inner cell components. 25 μm thick tantalum strips were used to contact the relevant cell components and establish the connection to the potentiostat. A picture of the assembled cell during illumination may be seen in Supplementary Figure S24.

Lab conditions

The following lab conditions were used, unless otherwise mentioned. The cathode of the PEC cell was fed by a humidified carbon dioxide stream: high-purity CO_2 flowed through a bubble humidifier, filled with Milli-Q water (resistivity > 18.2 MΩ∗cm), at a flow rate of 10 sccm. The bubble humidifier

could be heated, but it was generally kept at room temperature (~25 °C). A syringe pump pushed 1м KOH at a rate of 0.05 ml min^{-1} through the anode side of the PEC cell, and then into a liquid-gas separator, segregating the produced O_2 from the liquid feed. The separator was purged by a dry, high-purity nitrogen flow at 2 sccm to facilitate continuous product analysis. Current-voltage curves were all acquired in a two-electrode configuration; different scan rates were employed to evaluate the electrochemical (-2 to 3.2 V at 10 mV s^{-1}) and the photovoltaic (0 to 4 V at 200 mV s^{-1}) performance. Electrochemical impedance spectroscopy (EIS) spectra were recorded at 3 V between 5 MHz and 2 Hz, using a voltage amplitude of 10 mV. The PEC cell was illuminated by a solar simulator with an AM1.5G filter, providing an illumination intensity of 1 sun (0.1 W cm^{-2}). The light intensity was calibrated using a monocrystalline silicon reference solar cell.

Product analysis

The gas products were analyzed using two gas chromatographs (GCs) at the same time. On the cathode side, a GC from SRI Instruments (Multiple Gas Analyzer #5, 8610C), equipped with a thermal conductivity detector (TCD) and flame ionization detector (FID) plus methanizer, was used to analyze H_2 and CO concentrations. On the anode side, an Agilent GC (7890A) using a TCD was used to measure O_2 concentrations. Calibration curves were created using three to five standards for each gas component. The mass flow meters (Alicat Scientific), placed behind the GC outlets, captured potential leaks or CO_2 crossover through the membrane, allowing precise calculations of product amounts. The CO_2 utilization efficiency is calculated by dividing the molar flow of CO in the cathode outlet stream through the inlet CO_2 molar flow.

Conversion efficiencies

22

The solar-to-hydrogen (STH) efficiency is calculated by dividing the produced H_2 (minimum water splitting potential of 1.23 V at 25 °C, multiplied with the total current density and faradaic efficiency for H_2) by the illumination power density of 1 sun (0.1 W cm^{-2}):

$$STH = \frac{1.23\ V \times current\ density \times faradaic\ efficiency\ (H_2)}{0.1\ W\ cm^{-2}}. \tag{1}$$

The solar-to-CO efficiency is determined similarly. Here, the amount of produced CO and the minimum cell potential of 1.34 V required for its cathodic evolution, are considered:

$$Solar\text{-}to\text{-}CO = \frac{1.34\ V \times current\ density \times faradaic\ efficiency\ (CO)}{0.1\ W\ cm^{-2}}. \tag{2}$$

The respective faradaic efficiencies, which describe the fraction of total electrolysis current used to generate each gas product, are calculated based on the gas product amounts measured by the GCs. The combined solar-to-fuel (STF) efficiency may be calculated by adding the STH and solar-to-CO efficiencies. If the above-mentioned Fresnel lens is used, the illumination power density would need to be multiplied by the light concentration factor in order to calculate the correct solar conversion efficiencies.

Finally, the amount of energy used to produce H_2 and CO, divided by the net electrical energy supplied to the system, describes the energy/energetic efficiency (EE) towards the aforementioned products:[18]

$$EE_{H_2} = \frac{1.23\ V \times faradaic\ efficiency\ (H_2)}{full\ cell\ voltage}, \tag{3a}$$

23

$$EE_{CO} = \frac{1.34\text{ V} \times \text{faradaic efficiency (CO)}}{\text{full cell voltage}}.$$

(3b)

Surface Characterizations

The surface chemical composition was characterized by XPS and ISS on a Kratos Axis Ultra DLD system at room temperature. For XPS, a monochromatic Al Kα source (hv = 1486.6 eV) operated at 75W was used to excite the core level electrons of the material. Survey spectra were collected, with a pass energy of 160 eV, step size of 1 eV, and six sweeps each to obtain a good signal-to-noise ratio. The measurement was performed at a takeoff angle of 0° relative to the surface normal. Spectral fitting was conducted using CasaXPS analysis software. The ISS spectra were obtained using 0.92 kV acceleration at 1.0 mA and a 140° scattering angle. Scanning electron microscopy (SEM) and EDS were performed in a FEI Quanta 250 FEG system to evaluate the surface morphology and composition.

Acknowledgements

Conflict of Interest

The authors declare no competing interests.

References

[1]   D. Lüthi, M. Le Floch, B. Bereiter, T. Blunier, J.-M. Barnola, U. Siegenthaler, D. Raynaud, J. Jouzel, H. Fischer, K. Kawamura, T. F. Stocker, *Nature* **2008**, *453*, 379.

[2]   J. Hansen, D. Johnson, A. Lacis, S. Lebedeff, P. Lee, D. Rind, G. Russell, *Science* **1981**, *213*, 957.

[3]   V. Masson-Delmotte, P. Zhai, H.-O. Pörtner, D. Roberts, J. Skea, P. R. Shukla, A. Pirani, W. Moufouma-Okia, C. Péan, R. Pidcock, S. Connors, J. B. R. Matthews, Y. Chen, X. Zhou, M. I. Gomis, E. Lonnoy, T. Maycock, M. Tignor, T. Waterfield, *Global Warming of 1.5°C. An IPCC Special Report on the impacts of global warming of 1.5°C above pre-industrial levels and related global greenhouse gas emission pathways, in the context of strengthening the global response to the threat of climate change, sustainable development, and efforts to eradicate poverty* **2018**.

[4]   S. N. Habisreutinger, L. Schmidt-Mende, J. K. Stolarczyk, *Angew. Chem. Int. Ed.* **2013**, *52*, 7372.

[5]   L. Fan, C. Xia, F. Yang, J. Wang, H. Wang, Y. Lu, *Sci. Adv.* **2020**, *6*, eaay3111.

[6]   S. Y. Lee, S. Y. Chae, H. Jung, C. W. Lee, D. T. Le Nguyen, H.-S. Oh, B. K. Min, Y. J. Hwang, *J. Mater. Chem. A* **2020**, *8*, 6210.

[7]   M. Ebaid, K. Jiang, Z. Zhang, W. S. Drisdell, A. T. Bell, J. K. Cooper, *Chem. Mater.* **2020**, *32*, 3304.

[8]   J. S. DuChene, G. Tagliabue, A. J. Welch, X. Li, W.-H. Cheng, H. A. Atwater, *Nano Letters* **2020**, *20*, 2348.

[9]   K. Li, B. Peng, T. Peng, *ACS Catal.* **2016**, *6*, 7485.

[10]   K. Jiang, Y. Huang, G. Zeng, F. M. Toma, W. A. Goddard, A. T. Bell, *ACS Energy Lett.* **2020**, *5*, 1206.

[11]   D. M. Koshy, S. Chen, D. U. Lee, M. B. Stevens, A. M. Abdellah, S. M. Dull, G. Chen, D. Nordlund, A. Gallo, C. Hahn, D. C. Higgins, Z. Bao, T. F. Jaramillo, *Angew. Chem.* **2020**, *132*, 4072.

[12]   Q. Zhu, X. Sun, D. Yang, J. Ma, X. Kang, L. Zheng, J. Zhang, Z. Wu, B. Han, *Nat. Commun.* **2019**, *10*, 3851.

[13]   F. P. García de Arquer, C.-T. Dinh, A. Ozden, J. Wicks, C. McCallum, A. R. Kirmani, D.-H. Nam, C. Gabardo, A. Seifitokaldani, X. Wang, Y. C. Li, F. Li, J. Edwards, L. J. Richter, S. J. Thorpe, D. Sinton, E. H. Sargent, *Science* **2020**, *367*, 661.

[14]   D. Voiry, H. S. Shin, K. P. Loh, M. Chhowalla, *Nat. Rev. Chem.* **2018**, *2*, 173.

[15] J. Qiao, Y. Liu, F. Hong, J. Zhang, *Chemical Society Reviews* **2014**, *43*, 631.

[16] M. Behrens, F. Studt, I. Kasatkin, S. Kühl, M. Hävecker, F. Abild-Pedersen, S. Zander, F. Girgsdies, P. Kurr, B.-L. Kniep, M. Tovar, R. W. Fischer, J. K. Nørskov, R. Schlögl, *Science* **2012**, *336*, 893.

[17] J. F. Knifton, *J. Catal.* **1985**, *96*, 439.

[18] R. Küngas, *J. Electrochem. Soc.* **2020**, *167*, 44508.

[19] A. Y. Khodakov, W. Chu, P. Fongarland, *Chem. Rev.* **2007**, *107*, 1692.

[20] D. Li, E. J. Park, W. Zhu, Q. Shi, Y. Zhou, H. Tian, Y. Lin, A. Serov, B. Zulevi, E. D. Baca, C. Fujimoto, H. T. Chung, Y. S. Kim, *Nat. Energy* **2020**, *31*, 378.

[21] R. F. Service, *Science* **2020**, *367*, 1181.

[22] W. Tong, M. Forster, F. Dionigi, S. Dresp, R. Sadeghi Erami, P. Strasser, A. J. Cowan, P. Farràs, *Nat. Energy* **2020**, *467*, 367.

[23] J. H. Montoya, L. C. Seitz, P. Chakthranont, A. Vojvodic, T. F. Jaramillo, J. K. Nørskov, *Nat. Mater.* **2016**, *16*, 70.

[24] W.-H. Cheng, M. H. Richter, I. Sullivan, D. M. Larson, C. Xiang, B. S. Brunschwig, H. A. Atwater, *ACS Energy Lett.* **2020**, *5*, 470.

[25] M. Asadi, M. H. Motevaselian, A. Moradzadeh, L. Majidi, M. Esmaeilirad, T. V. Sun, C. Liu, R. Bose, P. Abbasi, P. Zapol, A. P. Khodadoust, L. A. Curtiss, N. R. Aluru, A. Salehi-Khojin, *Adv. Energy Mater.* **2019**, *9*, 1803536.

[26] M. Schreier, F. Héroguel, L. Steier, S. Ahmad, J. S. Luterbacher, M. T. Mayer, J. Luo, M. Grätzel, *Nat. Energy* **2017**, *2*, 17087.

[27] M. Schreier, L. Curvat, F. Giordano, L. Steier, A. Abate, S. M. Zakeeruddin, J. Luo, M. T. Mayer, M. Grätzel, *Nat. Commun.* **2015**, *6*, 7326.

[28] G. Gurudayal, J. Bullock, D. F. Srankó, C. M. Towle, Y. Lum, M. Hettick, M. C. Scott, A. Javey, J. Ager, *Energy Environ. Sci.* **2017**, *10*, 2222.

[29] F. Urbain, P. Tang, N. M. Carretero, T. Andreu, L. G. Gerling, C. Voz, J. Arbiol, J. R. Morante, *Energy Environ. Sci.* **2017**, *10*, 2256.

[30] V. Andrei, B. Reuillard, E. Reisner, *Nat. Mater.* **2020**, *19*, 189.

[31] T. Arai, S. Sato, T. Morikawa, *Energy Environ. Sci.* **2015**, *8*, 1998.

[32] M. Asadi, K. Kim, C. Liu, A. V. Addepalli, P. Abbasi, P. Yasaei, P. Phillips, A. Behranginia, J. M. Cerrato, R. Haasch, P. Zapol, B. Kumar, R. F. Klie, J. Abiade, L. A. Curtiss, A. Salehi-Khojin, *Science* **2016**, *353*, 467.

[33] T. A. Kistler, N. Danilovic, P. Agbo, *J. Electrochem. Soc.* **2019**, *166*, H656.

[34] L.-C. Weng, A. T. Bell, A. Z. Weber, *Energy Environ. Sci.* **2019**, *12*, 1950.

[35] S. Tembhurne, F. Nandjou, S. Haussener, *Nat. Energy* **2019**, *4*, 399.

[36] B. G. Pollet, A. A. Franco, H. Su, H. Liang, S. Pasupathi, in *Compendium of Hydrogen Energy*, Vol. 15, Elsevier **2016**, pp. 3–56.

[37] L. Jiang, G. Sun, in *Encyclopedia of Electrochemical Power Sources*, Vol. 78, Elsevier **2009**, pp. 390–401.

[38] R. P. Ramasamy, in *Encyclopedia of Electrochemical Power Sources*, Vol. 4, Elsevier **2009**, pp. 787–805.

[39] C. M. Gabardo, C. P. O'Brien, J. P. Edwards, C. McCallum, Y. Xu, C.-T. Dinh, J. Li, E. H. Sargent, D. Sinton, *Joule* **2019**, *3*, 2777.

[40] C. E. Creissen, M. Fontecave, *Adv. Energy Mater.* **2020**, *11*, 2002652.

[41] S. Verma, Y. Hamasaki, C. Kim, W. Huang, S. Lu, H.-R. M. Jhong, A. A. Gewirth, T. Fujigaya, N. Nakashima, P. J. A. Kenis, *ACS Energy Lett.* **2018**, *3*, 193.

[42] T. Haas, R. Krause, R. Weber, M. Demler, G. Schmid, *Nat. Catal.* **2018**, *1*, 32.

[43] A. Goyal, G. Marcandalli, V. A. Mints, M. T. M. Koper, *J. Am. Chem. Soc.* **2020**, *142*, 4154.

[44] L.-C. Weng, A. T. Bell, A. Z. Weber, *Physical chemistry chemical physics PCCP* **2018**, *20*, 16973.

[45] J. M. Perez, J. L. Large, in *Atomic Force Microscopy/Scanning Tunneling Microscopy 2*, Vol. 24182421 (Eds.: S. H. Cohen, M. L. Lightbody), Springer US. Boston, MA **1997**, pp. 233–239.

[46] N. Todoroki, H. Tei, H. Tsurumaki, T. Miyakawa, T. Inoue, T. Wadayama, *ACS Catal.* **2019**, *9*, 1383.

[47] R. Kas, K. K. Hummadi, R. Kortlever, P. de Wit, A. Milbrat, M. W. J. Luiten-Olieman, N. E. Benes, M. T. M. Koper, G. Mul, *Nat. Commun.* **2016**, *7*, 10748.

[48] J. Li, G. Chen, Y. Zhu, Z. Liang, A. Pei, C.-L. Wu, H. Wang, H. R. Lee, K. Liu, S. Chu, Y. Cui, *Nat. Catal.* **2018**, *1*, 592.

[49] B. Kim, H. Seong, J. T. Song, K. Kwak, H. Song, Y. C. Tan, G. Park, D. Lee, J. Oh, *ACS Energy Lett.* **2020**, *5*, 749.

[50] T. A. Kistler, M. Y. Um, P. Agbo, *J. Electrochem. Soc.* **2020**, *167*, 66502.

[51] W. T. Xie, Y. J. Dai, R. Z. Wang, K. Sumathy, *Renewable Sustainable Energy Rev.* **2011**, *15*, 2588.

[52] S. Y. Chae, S. Y. Lee, S. G. Han, H. Kim, J. Ko, S. Park, O.-S. Joo, D. Kim, Y. Kang, U. Lee, Y. J. Hwang, B. K. Min, *Sustainable Energy Fuels* **2020**, *4*, 199.

[53] H. S. Jeon, J. H. Koh, S. J. Park, M. S. Jee, D.-H. Ko, Y. J. Hwang, B. K. Min, *J. Mater. Chem. A* **2015**, *3*, 5835.

[54] Y. Sugano, A. Ono, R. Kitagawa, J. Tamura, M. Yamagiwa, Y. Kudo, E. Tsutsumi, S. Mikoshiba, *RSC Adv.* **2015**, *5*, 54246.

[55] Z. Chen, T. Wang, B. Liu, D. Cheng, C. Hu, G. Zhang, W. Zhu, H. Wang, Z.-J. Zhao, J. Gong, *J. Am. Chem. Soc.* **2020**, *142*, 6878.

[56] D. Ren, N. W. X. Loo, L. Gong, B. S. Yeo, *ACS Sustainable Chem. Eng.* **2017**, *5*, 9191.

[57] S. Garg, M. Li, A. Z. Weber, L. Ge, L. Li, V. Rudolph, G. Wang, T. E. Rufford, *J. Mater. Chem. A* **2020**, *8*, 1511.

[58] T.-J. Park, S. Banerjee, T. Hemraj-Benny, S. S. Wong, *J. Mater. Chem.* **2006**, *16*, 141.

[59] M. Pumera, A. Ambrosi, E. L. K. Chng, *Chem. Sci.* **2012**, *3*, 3347.

[60] C. M. Long, M. A. Nascarella, P. A. Valberg, *Environmental pollution (Barking, Essex 1987)* **2013**, *181*, 271.

[61] J. F. Geisz, R. M. France, K. L. Schulte, M. A. Steiner, A. G. Norman, H. L. Guthrey, M. R. Young, T. Song, T. Moriarty, *Nat. Energy* **2020**, *32*, 326.

[62] G. Sahara, H. Kumagai, K. Maeda, N. Kaeffer, V. Artero, M. Higashi, R. Abe, O. Ishitani, *J. Am. Chem. Soc.* **2016**, *138*, 14152.

[63] S. Toghyani, E. Afshari, E. Baniasadi, S. A. Atyabi, *Electrochim. Acta* **2018**, *267*, 234.

Table of Contents
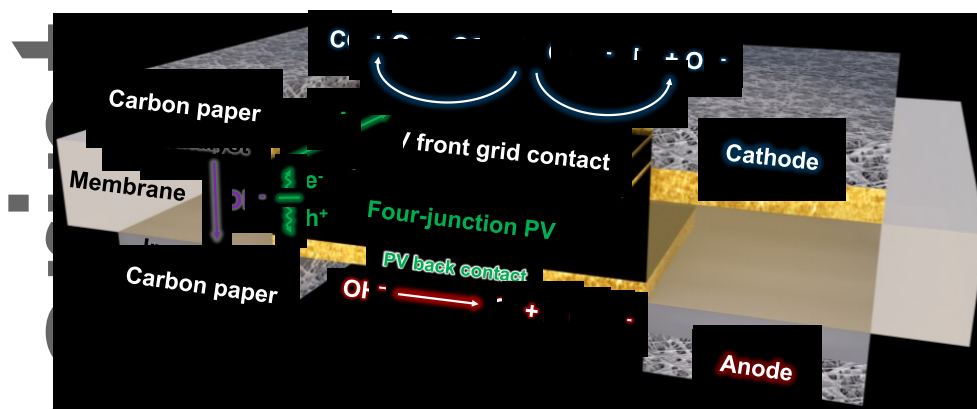
Photoelectrochemical conversion of carbon dioxide (CO$_2$) into fuels and chemicals is an appealing method to combat rising CO$_2$ concentrations in the atmosphere. A modular, fully-integrated device architecture is presented, following design principles developed for dark electrolysis and fuel cells. The result is a compact device, allowing for efficient and stable conversion of water and CO$_2$ into carbon monoxide and hydrogen (synthesis gas).

ToC Keyword: solar fuels